Investigating Errors of Wake Vortex Retrievals Using High Fidelity Lidar Simulations

Niklas Wartha*, Anton Stephan†, Frank Holzäpfel‡, Grigory Rotshteyn§
Institut für Physik der Atmosphäre, Deutsches Zentrum für Luft- und Raumfahrt, 82234 Oberpfaffenhofen, Germany

Wake vortex characterization algorithms for Light Detection and Ranging (lidar) measurements are vital for airport operation studies considering both efficiency of aircraft throughput and the related safety issue. To date the operational accuracy of algorithms such as the Radial Velocity (RV) method, particularly in turbulent atmosphere, has not been quantified thoroughly. In real lidar scans, the true flow field and the characteristics of the contained coherent structures, such as wake vortices, are unknown. Thus, the error of algorithms such as the RV method has not yet been considered beyond theoretical estimations. In this work we tackle the unavailability of a ground-truth by simulating virtual lidar instruments employing high fidelity Large Eddy Simulations (LES) of a landing aircraft. Within the numerical simulations the characteristics of the wake vortices are fully known, so that the accuracy of algorithms such as the RV method can be investigated and quantified. Virtual lidar scans generated by our proposed LES Lidar Simulator (LLS) focus on accurately representing the filtering effect of real lidar via a range gate weighing function. Comparisons to real lidar measurements and the simulated wake of the LES suggest that first accuracy estimations of the RV method can already be performed with the present LLS version. We observe that theoretical RV method characterization errors are significant underestimations, particularly the strength of vortices appears to be overestimated. These results manifest the necessity to investigate errors inherent to wake vortex characterization algorithms from lidar measurements also in further atmospheric conditions and aircraft landing scenarios.

I. Introduction

Detecting and characterizing coherent structures in Light Detection and Ranging (lidar) measurements can be performed via a variety of algorithms. Typically such algorithms are specifically engineered for an application, for instance for characterizing wake vortices as is the focus of this paper. Wake vortices are a by-product generated by any lift-producing aircraft [1] and can pose a hazard to following aircraft encountering these. Depending on the geometry of the aircraft the number of wake vortices can vary [2], however those wake vortices posing the highest risk to following aircraft are the primary wake vortices - they predominantly shed off the wing-tips and flap-tips. Aircraft, particularly during approach and landing, may be subject to wake vortices generated by previous aircraft given that the glide path between aircraft does not vary much [3] and experience so-called Wake Vortex Encounters (WVEs). The severity of a WVE depends on the circulation of the encountered vortex, the weight and wingspan of the encountering aircraft, the encounter direction, and the encounter altitude [4]. There is no definition for safe-to-encounter wake vortices, as a multitude of parameters are involved (see [4]), merely rules-of-thumb, experience, and relative arguments derived from similar WVEs can be applied.

Typically lidar instruments are installed at airports perpendicular to the runway to investigate wake vortices of landing aircraft. Wake vortex lidar measurements are conducted for studies such as investigating the effectiveness of devices (named plate lines) to mitigate wake vortices in ground proximity [5]. Alternatively wake vortex lidar measurements are needed for operational purposes as proposed in [6], where a lidar instrument is suggested for continuously obtaining real-time information about wake vortices over runways. Such studies contribute to introducing pair-wise dynamic aircraft separations at airports, which can enable efficient runway usage while maintaining the high safety standard, as suggested in the RECAT program introduced by Eurocontrol and the FAA [7]. Ultimately the RECAT program aims to

*PhD Candidate (Niklas.Wartha@dlr.de).
†Research Scientist.
‡Senior Scientist, Associate Fellow AIAA.
§Research Assistant.

adapt ICAO landing separations often considered too conservative [1], limiting the capacity of an airport, to separations between individual aircraft types while taking into account prevailing weather conditions. Past and future studies, such as those named above, require algorithms to retrieve wake vortex characteristics from the lidar measurements.

Several algorithms for characterizing wake vortices from lidar measurements exist. Typically the evaluation of wake vortices with these algorithms is limited to localizing the wake vortices and determining their strength via the circulation. Depending on the lidar device used to measure the wake of an aircraft, retrieval of wake vortex characteristics is performed using different algorithms. Two common analytical algorithms are the Velocity Envelope (VE) method [8, 9] for lidars with a beam wavelength of 2 μm and the Radial Velocity (RV) method [10, 11] for lidars with a beam wavelength of 1.5 μm. Further, recent efforts for wake vortex characterization include the usage of Artificial Neural Networks (ANNs) [12–14], primarily due to their independence of the lidar type and their fast processing speed. The primary problem of these algorithms is that their true error margins are unknown. The so-called ground-truth of the wake vortex characteristics delivered by these algorithms is unavailable - the real position and strength of the wake vortices are unknown - such that any conclusions drawn from analyses conducted with these algorithms should be considered with care. Algorithms such as the above mentioned typically report theoretical error margins derived from their underlying equations or in comparison to other algorithms, yet to the author's knowledge there are no empirical data for such error margins. Trust in systems and studies relying on lidar analysis will stay moderate as long as accurate error estimations can be formulated for the wake vortex characterization algorithms for lidar measurements.

In this work we therefore suggest to analyze wake vortices in simulated lidar measurements within a high fidelity Large Eddy Simulation (LES) of a landing aircraft (coupled with a Reynolds-Averaged Navier Stokes (RANS) simulation) rather than real measurements at an airport. Oppositely to the latter, the position and strength of all vortices within the simulated domain are fully known and algorithms such as the RV method can be compared to the ground-truth delivered by the LES. We suggest a LES Lidar Simulator (LLS) which can therefore be employed in any landing and atmospheric scenario. The LLS allows a full examination of the weaknesses and strengths of algorithms such as the RV method, which is the algorithm we focus on in this work. Note that the methods presented in this paper are analogous for comparative lidar processing methods for wake vortex measurements.

II. Methods

A. Lidar Measurements

Lidars aim to capture the movement of air particles, often termed aerosols, in the atmosphere. Consider Figure 1, a lidar emits a laser beam (indicated by the diagonal line) into a defined direction known as the Line of Sight (LOS). Many lidar types exist, herein we focus on pulsed coherent lidar, where spatiotemporal range gates along the beam are considered. To fully define the LOS, two positional arguments are used, the azimuth angle θ (in this work assumed zero or constant) and the elevation angle φ. On top of the these angles, a lidar beam has several range gates along its longitudinal direction, which define regions of measurement. The center of the range gate is taken as the range from the lidar instrument R. Wake vortex measurements with a lidar are of Range Height Indicator (RHI) type, that is, the azimuth angle is held constant (as sketched in Figure 1, perpendicular to the runway), while the elevation angle is varied and measurements along the longitudinal beam direction are taken (at the range gates). Due to this, a lidar can only determine the movement of aerosols away or towards the lidar. Figure 1 labels the two primary vortices generated by the aircraft flying out of the page using pairs of (y_c, z_c).

Processing of lidar measurements to radial velocities, as is common practice with wake vortex measurements, takes into account the normal distribution of a pulse of the lidar laser beam. The lidar detector receives a backscattered (or echo) signal of intensities in time. Through the pulse's time of flight, an estimation of the distance of the point of measurement along the LOS to the lidar instrument, R, can be retrieved. Application of the Fourier transform to the time signal within a range gate gives the backscattered signal in the frequency spectrum and allows, through consideration of the Doppler shift, obtaining the radial velocity at the peak of the spectrum. The spectra measured by a lidar can be described by Equation 1 [9], with $\bar{P}_S$ representing the normalized power of the echo signal averaged over microphysical parameters of the scattering aerosols, c giving the speed of light, T_W denoting the time window (effective width of the frequency resolution determining window in the measured spectrum), σ_P meaning the laser pulse duration, $W(t)$ giving the shape of the temporal pulse window (typically considered Gaussian), V_r representing the radial velocity, and λ giving the laser wavelength. Details on the derivation of Equation 1 can be found in [9].

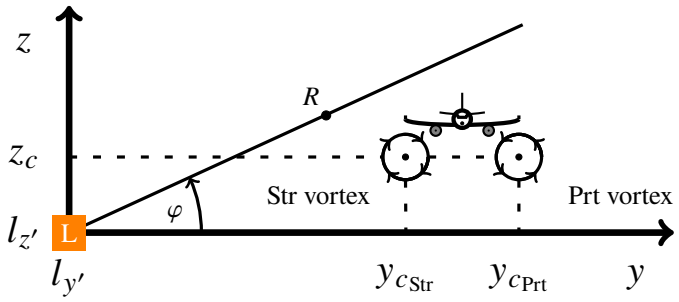

Fig. 1 Schematic of the lidar set-up with the starboard (Str) and port (Prt) vortices, where L represents the lidar placed in the LES domain [14].

$$\bar{S}(f) = \frac{2\bar{P}_S}{cT_W\sqrt{\pi}\sigma_P}\int_{-\infty}^{+\infty} dz \left| \int_{-\infty}^{+\infty} dt W(t) \exp\left[-\frac{(t-2z/c)^2}{2\sigma_P^2} - 2\pi j t \left(f - \frac{2V_r(R+z)}{\lambda} \right) \right] \right|^2 \tag{1}$$

B. Radial Velocity (RV) Method

Here we recapitulate details of the RV method previously introduced in [10]. The RV method is split into three parts, the first two parts deal with localizing vortices and the third part deals with defining their circulation. First the ranges of the vortex centers from the lidar R_c are obtained by evaluating the maxima of Equation 2.

$$D(R_j) = \sum_{k=1}^{K} \left[V_r(R_j, \varphi_k) \right]^2 \tag{2}$$

where K gives the total number of available LOS in a lidar scan, V_r the radial velocity of the aerosols from the perspective of the lidar, and φ the elevation angle of the respective LOS. To complete the localization of the vortices within the lidar scan, the elevation angle to the vortex centers φ_c is computed using the minimum and maximum radial velocities at the previously found R_c. The third characterization parameter, the circulation, is evaluated by employing the functional of Equation 3.

$$\rho(\Gamma) = \sum_{k=0}^{K} (V_r(R_c, \varphi_k) - \widetilde{V}_r(R_c, \varphi_k; \Gamma_1, \Gamma_2))^2 \tag{3}$$

where Γ is the circulation, Γ_1 and Γ_2 are arbitrarily chosen circulations and $\widetilde{V}_r$ is a modeled lidar scan. According to [10] the theoretical Root Mean Square Errors (RMSEs), assuming a Carrier-to-Noise Ratio (CNR) of 0.05, is 1.8 m, 0.21°, and 10.3 m^2/s for the range R_c, elevation angle φ_c, and circulation Γ, respectively. Theoretical estimates for Performance estimates for real measurement data, in particular for turbulent scenarios have not yet been extracted.

The RV method is implemented using LabVIEW. Both the vortex localization and the circulation determination are prone to further inaccuracies with this implementation, in addition to the errors inherent to the theory. Practical positioning errors arise from difficulties recognizing distinct peaks in $D(R_j)$ spectra. Further, noise and miscellaneous atmospheric turbulence smear the vortex profile for the selection of the elevation angle of a vortex. Practical circulation inaccuracies arrive from efficiency simplifications, where the model circulation solely covers a certain range with a specified step, thus the accuracy correlates with the selected circulation step.

C. Numerical Set-Up

Numerical simulations of landing aircraft have been investigated heavily by Stephan et al. [2, 15], in the current effort a great portion of methodology has been adopted and taken as a baseline for the implementation of the LLS. For further insight into the numerical methodology please see [15]. The following sporadically recapitulates the most crucial aspects of the numerical set-up for simulating the landing of a long range aircraft, within which the LLS is implemented.

1. Governing Equations

In this effort LES of a long range landing aircraft in high-lift configuration are computed by employing MGLET, an incompressible Navier-Stokes code developed at Technical University of Munich for solving the Navier-Stokes Equations (4) and continuity Equation (5) [16].

$$\frac{\partial u_i}{\partial t} + \frac{\partial (u_i u_j)}{\partial x_j} = -\frac{1}{\rho}\frac{\partial p'}{\partial x_i} + \frac{\partial}{\partial x_j}\left((\nu + \nu_t) 2 S_{ij}\right) \tag{4}$$

$$\frac{\partial u_j}{\partial x_j} = 0 \tag{5}$$

In the above u_i gives the velocity components for three spatial directions $i = 1, 2, 3$, the strain rate tensor is given by $S_{ij} = (\partial u_i/\partial x_j + \partial u_j/\partial x_i)/2$, and $p' = p - p_0$ represents the pressure deviation from a reference state p_0. Using a Lagrangian dynamic subgrid scale model [17], the kinematic viscosity is computed (the sum of molecular viscosity ν and eddy viscosity ν_t). A fourth-order finite-volume compact scheme solves Equations 4 and 5 [18]. The coefficients of the compact scheme are retrieved using a split-interface algorithm for the parallelization of the tri-diagonal system [19]. The incompressible Navier-Stokes equations are solved using a finite-volume approach [18]. Time integration is performed by employing a third-order explicit Runge-Kutta method.

2. RANS Flow Field Integration

Herein a one-way coupling of RANS and LES, as described by [20], is implemented in the landing scenario as introduced in [15]. While RANS simulations are accurate in simulating the flow around an aircraft [21], LES can simulate the effect of the atmosphere on the wake well [22, 23]. The wake of a long range aircraft in high-lift configuration is initialized by sweeping a high-fidelity RANS flow field of the named aircraft through the LES domain, enabling to simulate the evolution of wake vortices from generation until final decay [20]. Effectively, the RANS flow field represents a forcing term in Equation 4 of the LES. Thus, a fortified solution algorithm [24] is employed, delivering the resulting velocity field in the aircraft vicinity according to the weighted sum of Equation 6 as illustrated in Figure 2. The transition function between the LES and RANS flow fields is given by Equation 7, where α and β denote the slope and wall-distance of the RANS-LES transition, respectively.

$$\boldsymbol{V} = f(y)\boldsymbol{V}_{\mathrm{LES}} + (1 - f(y))\boldsymbol{V}_{\mathrm{RANS}} \tag{6}$$

$$f(y, \alpha, \beta) = \frac{1}{2}\left[\tanh \alpha \left(\frac{y}{\beta} - \frac{\beta}{y}\right) + 1.0\right] \tag{7}$$

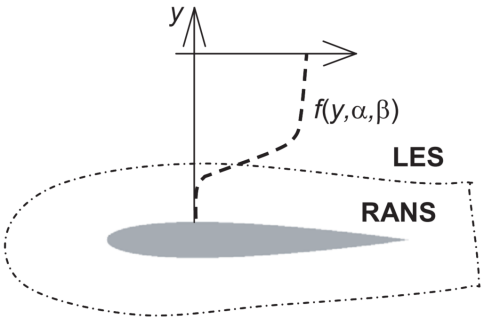

Fig. 2 Illustration of the weighting function coupling the RANS and LES velocity fields [20].

The RANS flow field of a 1/27 scaled model (wingspan of $b = 2.236$ m and aspect ratio $\Lambda = 9.3$) is computed by the DLR-TAU-code [25] from a steady compressible RANS simulation. For the wing-tip and flap-tip vortices, as well as the fuselage wake, adaptive mesh refinement is employed. The model chord based Reynolds number is $Re = 5.2 \times 10^5$ (two orders of magnitude lower than the real aircraft) at a flight speed of $U_\infty = 25$ m/s and a lift coefficient of $C_L = 1.4$. Conversely to [15], the RANS simulation is up-scaled post-simulation, such that real-life dimensions of the appropriate

long range aircraft are matched. This enables simulating lidar with real dimension and parameters, resulting in good comparability to real measurements and straightforward integration of other aircraft types. Through the post-simulation scaling (multiply dimensions by 27 and velocities by 3), we increase the Reynolds number to a realistic $Re = 42.1 \times 10^6$, the flight speed to $U_\infty = 75$ m/s, and the wingspan to $b = 60.3$ m (Λ remains unchanged). In order to not affect the CFL number by the scaling, the timestep is increased in contrast to [15].

Increasing the Reynolds number with the performed post-simulation scaling can cause the core radius of wake vortices to be represented too large compared to what is expected at such a Reynolds number. A numerical simulation of the full-scale model, a scaling 1:1 (no post-simulation scale-up) would produce more compact vortices. Furthermore, the effect of secondary vortices is changed. We nonetheless expect the dominant primary wake vortices to be comparable for the purpose of a virtual lidar. Due to the working principle of a lidar, the flow field it aims to capture is inherently smeared out and filtered such that mainly the primary wake vortices can be identified. In contrast, scaling effects are considered negligible, particularly given that both the RV method, as well as the ground-truth analyze the same flow field. A future study will investigate the impact of the post-simulation scaling on the wake of an aircraft further.

While the RANS flow field is computed on a refined unstructured grid, the LES domain is split in a structural grid. Thus, linear interpolation is conducted once before the wake initialization. We follow [15] to implement an aircraft glide path of 3.6° (while the angle of attack of the aircraft equals 5.5°). A steady RANS solution that is used to initialize the LES simulation is called a frame. For each LES timestep this frame is shifted in accordance to the aircraft movement. Given that the LES has discrete equidistant grid points, to realize the glide path multiple frames are required. The implemented glide path angle thus requires 16 frames to represent a movement of 16 horizontal grid points and one vertical grid point. To allow a smooth wake initialization, we double the frame number to 32 (with interpolation in between).

In this effort we normalize quantities using reference values for an elliptic load distribution as defined in [1]. This includes the root circulation $\Gamma_0 = (2C_L U_\infty b)/(\pi\Lambda) = 433.41$ m^2/s, the initial vortex spacing $b_0 = (\pi/4)b = 47.4$ m, the vortex descent velocity $w_0 = \Gamma_0/(2\pi b_0) = 1.46$ m/s, the characteristic time $t_0 = b_0/w_0 = 32.52$ s, and the characteristic vorticity $\omega_0 = 1/t_0 = 0.031$ s^{-1}. Normalized quantities are marked with an asterisk (*) in this text.

3. Computational Domain, Approach and Boundary Conditions

The approach and landing evolution of the aircraft wake is simulated in two parts, first a hybrid RANS-LES wake initialization is performed until touchdown (see Figure 3(a)), second the result of the first part is continued in a pure LES to simulate the wake evolution as shown in Figure 3(b). The boundary conditions of the numerical simulations are as follows: vertical faces are periodic, the top face follows a free-slip condition, and the bottom face is conditioned as no-slip. We avoid the aircraft entering its own wake by artificially reconnecting the vortex filaments generated at the start of the numerical simulation in a horse show fashion - such behavior is often seen in reality due to Crow instability [15].

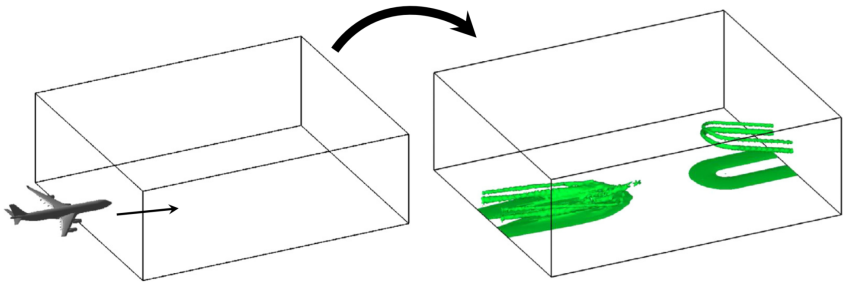

(a) Wake initialization until touchdown. (b) LES, vortex decay after touchdown.

Fig. 3 Illustration of the landing aircraft approach (a) displays the aircraft during wake initialization (b) shows the aircraft at the touchdown instance with the vortex filaments artificially reconnected [15].

At the touchdown instant, the lift of an aircraft is dramatically reduced, resulting in a major wake vortex reduction. In [15] it is assumed that lift completely vanishes at touchdown, thus the RANS flow field is removed as a forcing term in the LES. We disregard the white noise wake of the rolling aircraft after touchdown as suggested in [26]. The LES mesh spacing is uniform in all three spatial directions, $dx' = dy' = dz' = 0.54$. This mesh is coarser than reported in [15], as also the LES domain is scaled up to realistic dimensions.

The complete computational domain dimensions are $23.4b_0$, $5.8b_0$, and $2.2b_0$ in flight, spanwise, and vertical directions, respectively. The landing aircraft (nose) is initialized at $x' = 20.1b_0$, with the runway located along the x'-axis. The wake initialization of the aircraft occurs at an initial altitude of $z' = 1.5b_0$ and the aircraft is aligned with the runway i.e. $y' = 0b_0$. The aircraft touchdown occurs at $x' = 17.6b_0$, corresponding to $t^* = 0.4$.

D. Tracking Vortices in LES

The primary difficulty of detecting and characterizing wake vortices in lidar scans stems from only having the radial velocity component to the lidar of the flow field available. Conversely, when the full LES simulation is available for characterizing wake vortices, far more variables are at hand. Different criteria for detecting wake vortices in turbulent environment have been investigated in detail in [27]. A combination of the vorticity and pressure suffice to detect the primary wake vortices via global extreme values of $\omega_x p^\kappa$, where ω represents the vorticity, p the pressure, and $\kappa > 0$ a weighting coefficient [28]. Averaging and box constraints reduce effects of disturbances and the counter-rotating wake vortex of the pair. Once the position of a vortex is found, the circulation is computed at that location. The vortex intensity of large aircraft primary wake vortices is often characterized by $\Gamma_{5-15} = 0.1 \int_{5\mathrm{m}}^{15\mathrm{m}} \Gamma(r)dr$, where the circulation around a radius r, centered at the tracked vortex location, is $\Gamma(r) = \oint \boldsymbol{u} \cdot d\boldsymbol{s}$ [1, 29]. In this work we consider the results obtained using this method as the ground-truth.

E. LES Lidar Simulator (LLS)

The idea of simulating lidar instruments is not new, for instance Sallab et al. [30] and Manivasagam et al. [31] have previously coded lidar simulators for autonomous driving. Recently, also in atmospheric observation a first lidar simulator has been implemented by Robey et al. [32]. As part of LES post-processing a first basic approach of such simulator for wake vortex numerical simulations has been investigated by Stephan et al. [2]. To the author's knowledge a lidar simulator for wake vortex measurements fully embedded in the LES has previously not been presented. Thus, we propose the LLS used for evaluating the accuracy of currently available lidar scan processing algorithms. Principle implementations and assumptions strongly correlate with those found in [32] and aim to represent, in a simplified manner, the underlying lidar Equation 1. Given the nature of LES and the herein chosen spatial discretization, the resolution is insufficient to explicitly simulate the optical lidar measurement of scattered aerosols. However if we focus on the principal effects of volume averaging and reconstruction over the scanning volume, those scales LES can support. Lidar measurements can be assumed to be volume averages. Thus, the heart of the LLS is a Range Gate Weighting Function (RWF) suggested in [32].

The LLS can be broken down into two main components: (1) retrieval of the radial velocities along the LOS, and (2) application of a RWF. Specifications of the instrumentation and positioning with respect to the LES domain are detailed in (3). The following assumes pulsed coherent Doppler lidar similar to the Leosphere WindCube 200S (1.543 µm).

1. Radial Velocity Retrieval

A consequence of the lidar working principle is that it can solely retrieve flow velocities in the direction of its laser beam i.e. along the set LOS. Thus, aerosols moving away from the lidar are marked with a positive sign and aerosols towards the lidar are marked with a negative sign. As a result, the radial velocity of lidar measurements is often called LOS velocity. In the LES, along all three spatial directions the flow velocity vector $\boldsymbol{u} = [u, v, w]^T$ is computed at each node and timestep dt'. A lidar performing RHI measurements continuously changes its LOS according to a set scanning rate ω_S between a minimal and maximal elevation angle φ_- and φ_+, respectively. The laser beam of the lidar moves at the speed of light, it is therefore safe to assume that measurements along one LOS are instantaneous and thus at the same point in time. Although the lidar continuously sweeps up and down between φ_- and φ_+, in practice it seems as if at t_1 a recording of the velocities at the appropriate range gates belonging to a LOS is taken. Thereafter the elevation angle is changed as dictated by ω_S, after which at t_2 and a new (seemingly stationary) elevation angle, a recording of velocities at the appropriate range gates belonging to this next LOS is taken. In essence, this leads to a certain time dt required by the lidar to change between two LOS. In the rarest of cases, the timestep of the lidar and LES match i.e. $dt = dt'$. Instead usually $dt \neq dt'$ where $dt' << dt$, such that the LLS does not make use of every LES timestep. The herein presented LLS also does not perform temporal interpolation beyond nearest-neighbor interpolation.

The LES wall time T' is only available in discrete equidistant temporal points according to dt'. Similarly, the LLS wall time T is only available in discrete equidistant temporal points according to dt. When $|T - T'| \leq dt'/2$, the LLS is activated. Rarely the spatial position of a desired point (where we want to know the radial velocity) in the flow matches

a node of the LES mesh. Bilinear interpolation is used to obtain $\boldsymbol{u}$ at the requested point in the domain. Thereafter, the radial velocity seen by the lidar, V_r is computed by projecting $\boldsymbol{u}$ onto the lidar beam unit direction vector $\hat{\boldsymbol{b}}$ according to Equation 8. In this effort we assume the RHI lidar scans to be perfectly perpendicular to the runway i.e. $y \parallel y'$, thus the velocity component u can be disregarded for the LLS.

$$V_r = \hat{\boldsymbol{b}} \cdot \boldsymbol{u} = v \cos\varphi + w \sin\varphi \tag{8}$$

For a variety of reasons, such as safety but also focusing of the lidar instrument, during measurement campaigns lidar instruments are often located further away from the runway. In an effort to allow larger distances between the lidar and the runway, without having to simulate vast amounts of flow domain which have placeholder characteristics, we implemented a lidar scan padding method that allows for the lidar to be placed outwith of the LES domain. Consider a lidar measurement window under- and overshooting the LES domain as shown in Figure 4, the following rules apply for obtaining appropriate LLS radial velocities outside of the LES domain: In field 0 values of $\boldsymbol{u}$ are directly retrieved from the appropriate position within the LES domain. The same cannot be done for fields 1 to 5. The LLS considers a straightforward padding of the relevant scan regions. In the horizontal regions outwith of the domain i.e. field 1 and 2, the z-component of the desired measurement point is kept, while the y-component is changed to the lowest node in the domain y'_- and highest node in the domain y'_+, respectively. Effectively, this copies $\boldsymbol{u}$ at the domain boundaries to points of the same z. Similarly field 3 operates in the vertical sense, copying $\boldsymbol{u}$ from y and z'_+. Lastly, field 4 and 5 copy values from (y'_-, z'_+) and (y'_+, z'_+), respectively. This lidar scan padding approach is assumed appropriate given that with realistic lidar positions along the LES domain, measurement points in fields 1-5 are rare and typically where no relevant flow features are found.

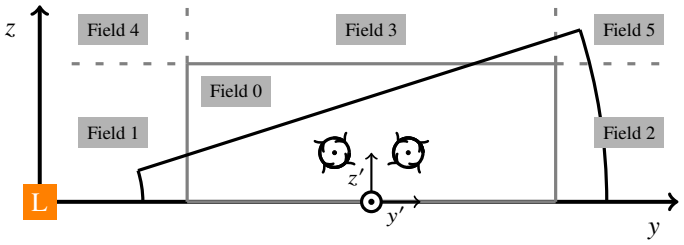

Fig. 4 Schematic of the lidar and LES coordinate systems. In gray the LES domain is drawn, in black the measurement window of the lidar. Field 0 represents the region where velocities can be retrieved from the appropriate location in the LES domain. Fields 1 to 5 represent regions where flow field padding is applied.

2. Range Gate Weighting Function (RWF) Application

In reality various factors affect the echo signal detected by a lidar, including: aerosol type, size and their density distribution, as well as, atmospheric conditions such as humidity, fog, and precipitation [33–35]. Furthermore, the CNR is not considered at this stage of the LLS. The primary tool to model the working principle of a wind lidar is to implement a RWF on the artificially retrieved lidar measurements by the LLS. In a number of works this has shown to approximate the sampling procedure of a lidar well [32, 36–38]. This approach can be compared to the application of a smoothing low-pass filter [32], smearing out the actual flow field. Details of the RWF application can be found in [32], below we review the methods necessary for this work.

Consider a LOS at a fixed elevation angle φ, along which we have a target distance R where we want to retrieve the radial velocity as would be measured in reality $\bar{V}_r$. A weighted volume average of V_r along the LOS direction about R is computed in the following. Given that the longitudinal dimension of a lidar beam is far greater than its width, a one dimensional line integral is sufficient. Equation 9 showcases how the weighting function ρ is convoluted to the projected flow velocities V_r computed in the previous section (from the LES solution). Therefore, ρ is a normalized RWF such that the total applied weight is unity and flow velocities are not scaled. For the implementation into the LLS a numerical approximation of the integral suffices. Hence, the continuous weighted average is restricted to a discrete weighted average as presented in [32]. The implemented quadrature formulation is a normalized midpoint rule, where additional equidistant points s_i along the LOS around R are retrieved from the LES ($s_i = 0$ at R). These additional points are restricted by $[-\hat{R}, +\hat{R}]$, neglecting the influence the Gaussian distribution tails and therefore necessitating the presented normalization in Equation 9. In the present effort, the equidistant points are 1 m apart (as in [32]) and $\hat{R} = 30$

m to preserve computational efficiency while ensuring small Gaussian distribution tails. Upcoming investigations will explore the large breath of options for choosing the additional points employed in the quadrature formulation.

$$\bar{V}_r(R) = \int_{-\infty}^{+\infty} \rho(s) V_r(R+s) ds \approx \sum_k \frac{h_k \rho(s_k)}{\sum_i h_i \rho(s_i)} V_r(R+s_k) \tag{9}$$

Pulsed lidars are considered in this work, such that ρ is given by Equation 10 - the convolution of the range gate profile with the pulse profile [36]. The pulse shape $g(s)$ is assumed to follow a Gaussian distribution and χ represents a top-hat normalized indicator function [32, 39]. The pulse can be expressed by the full-width half-maximum (FWHM) τ where $\tau = 2\tau_s/c$ (see Equation 11), and the indicator function for a range gate δR (in time represented by τ_m) is given by Equation 12, where $\delta R = c\tau_m/2$.

$$\rho(R) = \int_{-\infty}^{+\infty} g(R-s)\chi(s) ds \tag{10}$$

$$g(s) = \frac{2\sqrt{\ln 2}}{\tau_s \sqrt{\pi}} \exp\left(-4 \ln 2 \frac{s^2}{\tau_s^2}\right) \tag{11}$$

$$\chi(s) = \begin{cases} \frac{1}{\delta R} & , s \in \left[-\frac{\delta R}{2}, \frac{\delta R}{2}\right] \\ 0 & , \text{else} \end{cases} \tag{12}$$

Substitution of Equations 11 and 12 allows solving the integral of Equation 10, yielding the expanded form presented with Equation 13 as found in [32] and used for the computation within the LLS.

$$\rho(R) = \frac{1}{c\tau_m} \left[\text{erf}\left(\frac{4\sqrt{\ln 2}}{c\tau} R + \frac{\tau_m \sqrt{\ln 2}}{\tau} \right) - \text{erf}\left(\frac{4\sqrt{\ln 2}}{c\tau} R - \frac{\tau_m \sqrt{\ln 2}}{\tau} \right) \right] \tag{13}$$

3. LLS Specifications

The LLS of this work aims models the Leosphere WindCube 200S with laser wavelength $\lambda = 1.54\ \mu$m. Parameter values required to model the lidar without LLS are given in Table 1. Furthermore, this table gives the positioning of the simulated lidar instruments in terms of b_0 and with respect to the LES domain as seen in Figure 4, where $x' = 0$ is located at the boundary of the flow direction, behind the aircraft flying out of the page. This work simultaneously simulates multiple lidars, these have equivalent specifications, differing only in their x' - position.

Table 1 Variable LLS parameters and their corresponding values for the present work.

	Leosphere WindCube 200S
Number of lidars	5
Scanning rate ω_S (°/s)	4
Minimum elevation angle φ_- (°)	0
Maximum elevation angle φ_+ (°)	20
Minimum range gate R_- (m)	30
Maximum range gate R_+ (m)	530
Range gate spacing δR (m)	3
x'- direction lidar position $l_{x'}$ (-)	$(2.2, 6.8, 11.4, 15.9, 20.5)b_0$
y'- direction lidar position $l_{y'}$ (-)	$-5.9b_0$
z'- direction lidar position $l_{z'}$ (-)	$0b_0$
Temporal range gate τ_m (ns)	200
FWHM pulse width τ (ns)	140
Angular resolution $\delta\varphi$ (°)	0.2

III. Results

A. Numerical Simulation

The four phases of wake vortex evolution [40] - the near field, extended near field (roll up phase), mid/far field (vortex phase), and decay phase - can all be identified in the LES as well as [15]. Investigations in [2] show that a number of different wake vortices are generated by an aircraft, with the most prominent being the wing-tip and flap-tip vortices. Figure 5 shows numerical simulations at points in time during approach (Figure 5a) and touchdown (Figure 5b). Particularly during approach, the wake vortex filaments generated by the wing-tips and flap-tips are visible in the mid/far field. Further behind the aircraft, on both sides, the wing-tip (more prominent) and flap-tip vortex filaments are found to rotate around one another until they merge at an even longer distance aft the aircraft. Also visible is the vorticity induced on the ground by both the bound vortex of the aircraft and the vortex filaments [41].

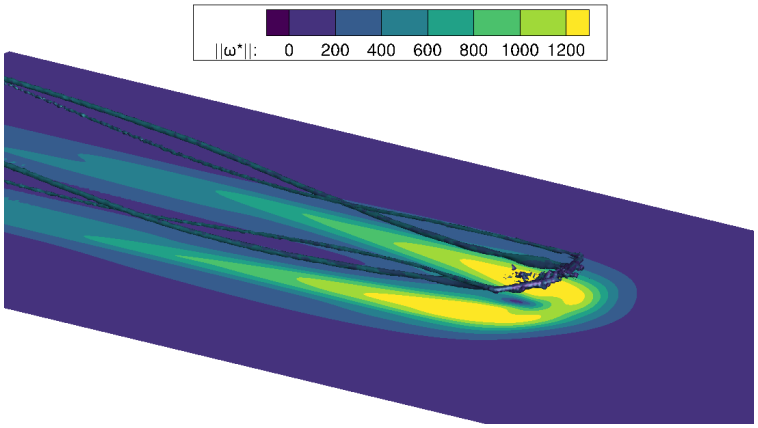

(a) $t^* = 0.31$

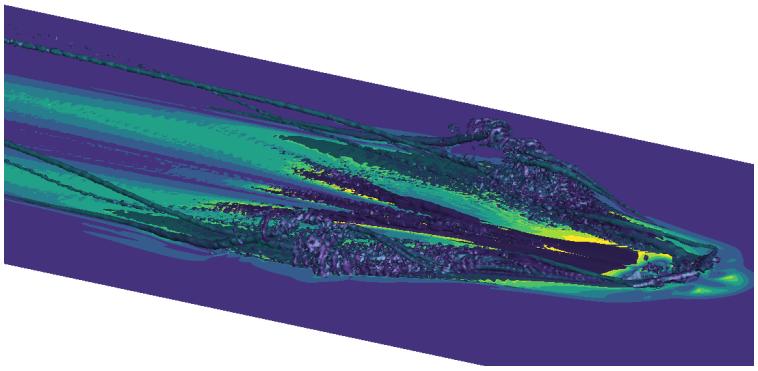

(b) $t^* = 0.40$

Fig. 5 Aircraft landing during approach and touchdown. Iso-vorticity surface $||\omega^*|| = 425$ colored with vorticity in the flow direction.

Besides the touchdown effects observed in Figure 5b, we also notice the out- and downward path the vortices have taken in comparison to Figure 5a. This hyperbolic motion is characteristic for wake vortices in ground proximity, given their interaction with secondary vortices which detach as a result from the induced shear layer mentioned above. Even a re-bound of the primary wake vortices is possible [42]. During touchdown and very-near ground altitudes, the interaction of the wake and the ground vorticity layer is highly turbulent. Shortly afterwards the bound vortex vanishes as no further lift is generated after touchdown, such that the free ends of the vortex filaments interact with the ground too.

Temporal wake vortex evolution is studied in Figure 6. A vertical slice is placed in the LES domain at the location of virtual lidar 1 (see Table 1). The slice is colored with the vorticity magnitude to visualize the wake vortex behavior we expect LLS scans to capture. Figure 6 is dedicated to post-touchdown wake development. Figure 6a captures the instant

of touchdown, individual vortices from the wing-tips and the flap-tips are still visible, where the more prominent vortices originate from the former. Throughout Figures 6b and 6c the motion of the vortices at $x' = 2.2b_0$ is out- and downward. As theory suggests, the vortices making up the primary vortex pair mutually induce a downward velocity upon each other, also causing the outward diverging trajectory close to the ground. Up until this point in time, the wing-tip vortices and flap-tip vortices are independently recognizable, however in Figure 6d their interaction becomes evident as they merge into one large vortex. The illustrated iso-vorticity surface suggests this to be a highly turbulent mechanism, after which the strength of the vortices is reduced (see Figures 6d to 6f). The temporally later figures also show the primary vortex pair coming close to the vertical boundaries of the LES domain, after which the vortices dramatically rebound and begin to move back inward of the domain (see Figure 6e). Wake vortex rebound is expected in ground proximity, however inward motion is uncommon. Considering the numerical set-up of this work, the observed vortex pair behavior is not without foundation. We recall that the vertical faces of the LES domain are periodic, such that when the vortices are close enough to the domain boundaries, they are approached by an image vortex circulating in the opposing sense. Effectively, this generates two new vortex pairs - each real vortex is paired with an image vortex of opposing circulation on the vertical faces. These follow the same physical principles as the original primary vortex pair discussed above. However, in comparison to that original vortex pair these imaginary vortex pairs are located in the opposite way to one another, such that the vortex pair trajectories are upward and also outward (from the vortex pair perspective). Thus, the original vortex pair convects upward and inward the LES domain. At a critical point, the image vortices are once again far from the primary wake vortices, such that the main interaction occurs anew between the original vortex pair. This pattern unavoidably repeats until the strength of the primary vortices is too low and their coherency is lost - identifying vortices in Figure 6f is already not trivial. Future implementations of the LLS shall therefore include far wider LES domains to avoid, or at a minimum delay, this reoccurring behavior until the wake vortices are of negligible strength.

The above qualitatively discussed behavior is confirmed in Figure 7 which plots the characteristic wake vortex parameter values versus the characteristic time for the first three lidar positions (recall Table 1). Focusing on lidar position 1 first, the lateral movement (top of Figure 7) of both the starboard and port vortex can be seen to be outward, after which it is inward, followed by another outward movement. This confirms our previous observations of vortex motion, however we also notice that while the first outward convection occurs roughly within 1.5 characteristic time units, the following inward motion takes roughly 2 characteristic time units, and the last visible outward convection travels at an even slower rate. If instead focusing on the vertical vortex trajectories (middle of Figure 7), roughly 1.5 full upward and downward cycles can be observed within the same time frame. The initial vortex pair descend is nearly not recorded, as it starts from a moderate altitude (in comparison to later rebounds), and the initial descend is rapid in comparison to the following motions. Further, erroneous data points are disregarded (typically young vortices are just being generated and rolling up), and for computational efficiency reasons only every 200 LES timesteps data are saved. Lastly, the circulation plotted at the bottom of Figure 7 is discussed, once again with the focus on lidar position 1. The initial circulation is just above the root circulation, this is untypical [15]. The applied up-scaling of the RANS model (see Section II.C.2) can result in vortex cores that are larger than expected at this Reynolds number, which could explain the larger initial circulations and reiterates the need for further investigations into this matter. The circulation magnitude rapidly decreases within the first three characteristic time units. As time progresses further the circulation decreases more moderately - these two vortex decay phases are widely accepted in the literature [1].

Lastly, we compare the impact of the lidar positions in the LES. Three lidar positions are printed in Figure 7, where lidars 1 and 3 are associated to the virtual measurement plane first and last crossed by the aircraft, respectively. Furthermore, the aircraft altitude is highest at the virtual lidar 1 and lowest at lidar 3. The trajectories of the port and starboard vortices indicate more extreme movement where the ground effect is higher, namely vortices captured by virtual lidar 3 move more prominently than those captured by virtual lidars 1 and 2. The vortex strength is seen to be less affected by the lidar position. The vortex strength at young vortex age recorded at virtual lidar 3 is far below the vortex strength measured at virtual lidars 1 and 2 during the same time. We expect a virtual lidar measurement plane which is passed later to record vortices of lower strength in comparison to a virtual lidar measurement plane passed earlier. However, virtual lidar 3 follows this theory only during young vortex age. At older vortex age, vortex strengths are nearly indistinguishable between the different virtual lidars. Vortices captured at virtual lidar 3 are subject to greater ground effects than at virtual lidar 1, at the same time they are also younger. It can thus be argued that the ground and vortex age effects counteract one another. Nonetheless, the initially low vortex strength at virtual lidar 3 requires further analysis.

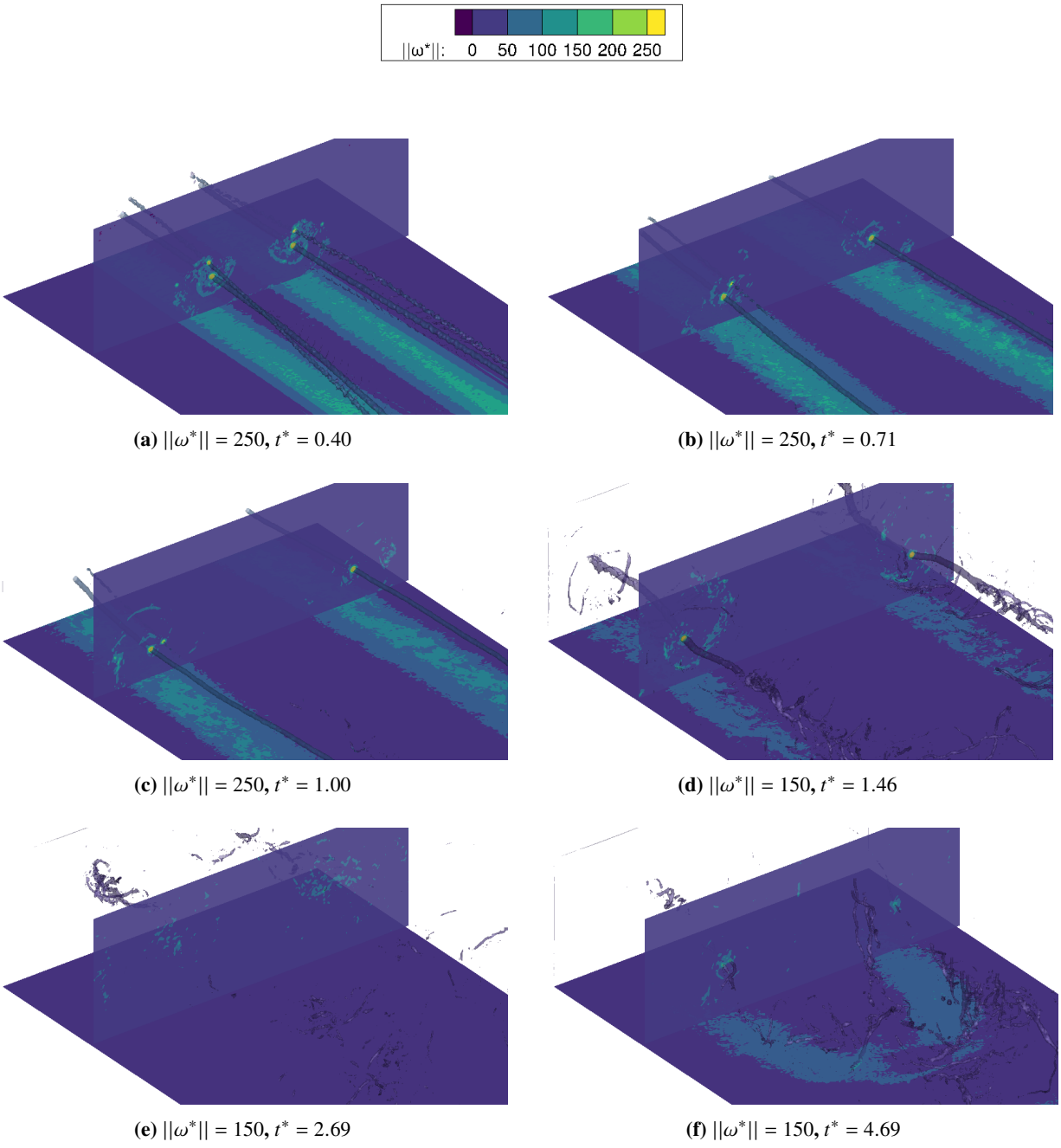

(a) $||\omega^*|| = 250$, $t^* = 0.40$ **(b)** $||\omega^*|| = 250$, $t^* = 0.71$

(c) $||\omega^*|| = 250$, $t^* = 1.00$ **(d)** $||\omega^*|| = 150$, $t^* = 1.46$

(e) $||\omega^*|| = 150$, $t^* = 2.69$ **(f)** $||\omega^*|| = 150$, $t^* = 4.69$

Fig. 6 Aircraft wake after touchdown. Iso-vorticity surface $||\omega^*||$ varies for visibility purposes (see subcaptions) and is colored with vorticity in the flow direction. The colorbar given is only valid for the vertical slice at lidar position 1 ($x' = 2.2b_0$), other components of the figure are colored according to the colorbar given in Figure 5.

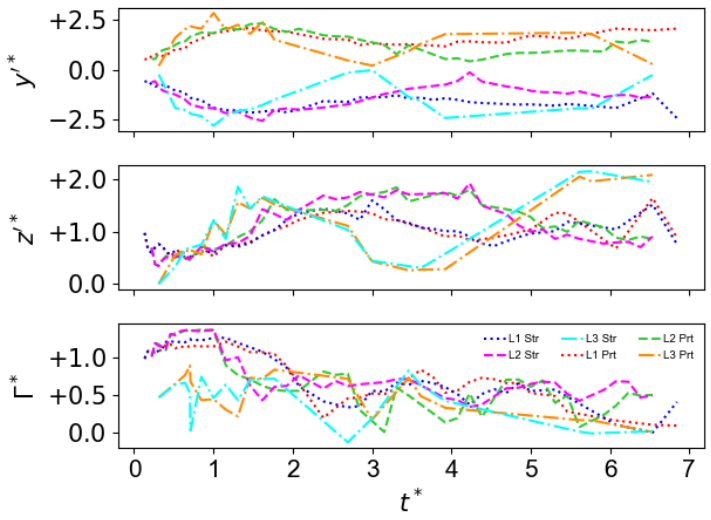

Fig. 7 Starboard (Str) and port (Prt) vortex position and circulation (Γ_{5-15}) distribution for lidar positions 1-3 (L1-L3) with respect to time. The circulation sense is disregarded in this figure.

B. LES Lidar Simulator (LLS) Scans

This section showcases and discusses LLS scan retrievals of the five virtual lidars. Scans are depicted in their natural polar form, via range and elevation angle, and the radial velocity. For visualization purposes velocities are capped at −10 m/s and +10 m/s, where velocities outwith these boundaries are replaced by the appropriate boundary value. LLS scans shown in Figure 8 are the temporally second LLS scans at each lidar position after the numerical simulation has been started. Thus, first LOS at high elevation angles are recorded, followed by LOS at lower elevation angles. Although these LLS scans are retrieved at the same points in time, they showcase different phenomena. The discrepancy arrives from the different locations along the LES domain x'- dimension.

With the aircraft nose initialized at $x' = 20.1b_0$ in the LES domain, according to Table 1 the virtual lidar measurement planes are passed by the landing aircraft in the following order: lidar 5, lidar 1, lidar 2, lidar 3. The measurement plane of virtual lidar 4 is only passed after the aircraft has landed. At $t^* = 0$ the aircraft is about to enter the measurement plane of virtual lidar 5. The primary wake vortex pair contained in Figure 8a can straightforwardly be identified therein. The individual vortices appear vertically stretched in comparison to LLS scans generated at following lidar positions. We observe that until $t^* = 0.31$ also virtual lidar measurement planes 1 and 2 have been flown through by the simulated landing aircraft - a full vortex pair is visible in these LLS scans (Figures 8b and 8c). Instead, Figure 8d depicts that during $t^* = 0.16 \rightarrow 0.31$ virtual lidar 3 only captures the lower half of the vortex pair, indicating that as the recording of virtual lidar 3 is taking place its measurement plane is passed. When $\varphi \gtrapprox 3°$, no wake vortices can be seen yet, however when $\varphi \lessapprox 3°$, the distinctive lower half of a wake vortex pair can be recognized. The LLS scan recorded by virtual lidar 4 (Figure 8e) does not capture any wake vortices as it is located beyond the touchdown point. The observations made in Figures 8d and 8e confirm the correct implementation of the LLS. In correlation with the order in which the virtual lidar measurement planes are passed (lidar $5 \rightarrow 4$), the vertical stretching of vortices reduces. At lidar position 5 vortices are oldest, such that they are less coherent than those observed at the other virtual lidars at the equivalent instant in time. Equally, the mutual descent of the vortex pair is most prominent in Figure 8a. With the LOS being recorded in a decreasing φ fashion, vortex stretching can occur. The presented LLS scans replicate this phenomenon observed in real measurements well [43].

For reference a scan from a lidar measurement campaign at Vienna International Airport (for details on the campaign see [5]) using the Leosphere WindCube 200S and specifications from Table 1 is visualized in Figure 9. Two major differences between the LLS scans of Figure 8 and the real measurement lidar scan can be observed: First, the atmosphere of the measured scan is far more turbulent than the atmosphere in the LES, evident from the measurement artifacts in the corners of Figure 9. Second, radial velocities seen in the real lidar scan appear lower than those of the LLS scans, suggesting that in reality the averaging and resulting filtering of the lidar spectra occur in a prominent manner. The neglecting of the CNR values in the LLS could be associated with, inter alia, the lack of noise and higher radial

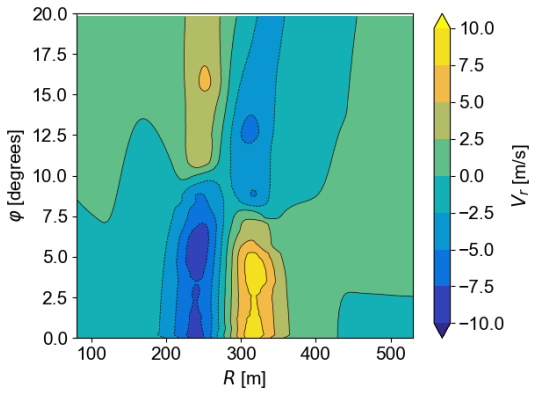

(a) Virtual lidar 5

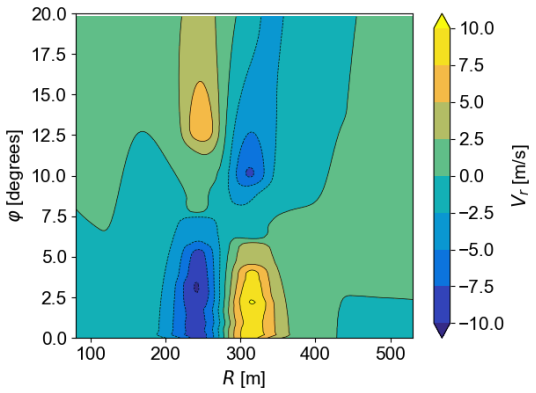

(b) Virtual lidar 1

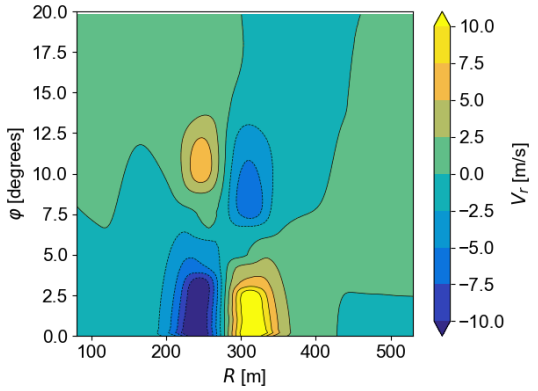

(c) Virtual lidar 2

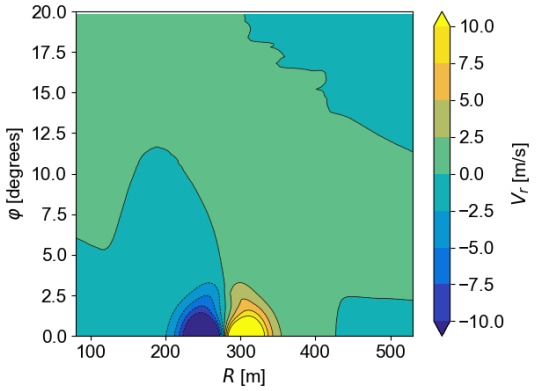

(d) Virtual lidar 3

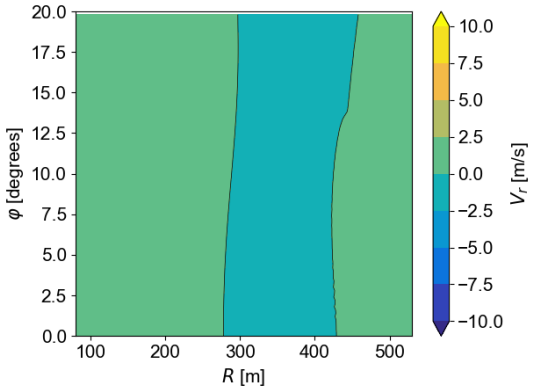

(e) Virtual lidar 4

Fig. 8 LLS scans at $t^* = 0.16 \rightarrow 0.31$ for the lidar positions 1 to 5 and parameters described in Table 1. LLS scans are ordered with respect to the aircraft passage. For this particular set of LLS scans, the individual LOS are generated in decreasing φ fashion.

velocities in the LLS scans. Nonetheless, this comparison of the LLS scans and the measurement scan shows that the LLS can produce near-reality lidar scans. Particularly for analyzing the accuracies of lidar scan processing methods for wake vortices, such fidelity of lidar scans can provide insight into methodological deficiencies of these processing methods under near ideal atmospheric conditions.

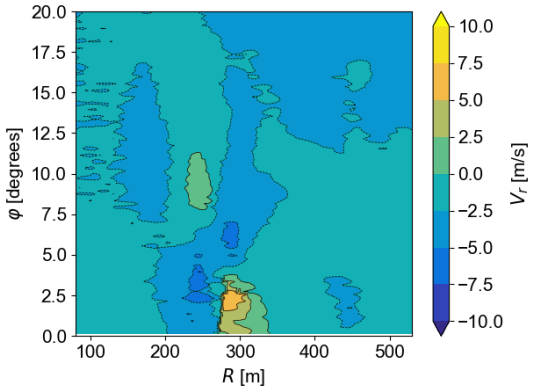

Fig. 9 Measured lidar scan from a 2019 campaign at Vienna International Airport using the Leosphere WindCube 200S of a Boeing 777-200 at young vortex age [5].

Further analysis in this section focuses on the temporal evolution of the LLS scans. For this purpose we focus on a single lidar position, namely lidar position 2. Figure 10 displays a sequence of temporally ordered, but not necessarily consecutive, LLS scans in the Cartesian coordinate system (avoiding scaling effects). Note that labels and circulation values within the figure are analyzed further in Section III.C.

Tracing the trajectory of the wake vortex pair starts at the earliest LLS scan shown in Figure 10a. Here, a prominent wake vortex pair can be identified straight after the long range aircraft has fully passed the virtual measurement plane of lidar 2. Conversely to Figure 6, the secondary vortices from the flap-tips are not visible. Such behavior is expected as a lidar, as well as the LLS (using the RWF), smear out or filter the measured flow field. Therefore, physically more prominent structures, such as the primary vortices from the wing-tips overshadow less prominent structures, such as those generated by the flap-tips. In the following three LLS scans (Figures 10b-10d), the typical behavior of a wake vortex pair in ground vicinity (previously highlighted in Section III.A) can be observed. First, the pair descends as each vortex induces a downward velocity onto the counter-rotating vortex. As the altitude of the vorticies decreases, the pair begins to laterally diverge i.e. the vortices follow a diverging hyperbolic trajectory. The vortices weaken in Figure 10d in comparison to the earlier LLS scans. The considerably large difference in time between the LLS scans in Figure 10e and 10f is not chosen arbitrarily. With the second batch of LLS scans, represented by Figures 10f-10h, we aim to address a current shortcoming of the present LLS implementation (also previously addressed in Section III.A). Between the LLS scans shown in Figures 10d and 10e, the vortex pair moves upwards - such rebound is not uncommon in ground vicinity. However, the vortex spacing decreases and in the temporally later scans a recurrence of the previously described physical mechanism occurs: the vortex pair moves in a down- and outward motion. The primary difference to the first cycle of this motion - when we still physically expect this behavior - is the strength and coherence of the vortices. During the second batch of LLS scans, both the circulation value and coherency diminish in comparison to the first batch of LLS scans, confirming what we have previously observed in the LES (see Figure 6).

In the Cartesian LLS scans, a side effect of the padding method can be observed. For instance in Figure 10c (but similar observation can be made in the other scans) we can clearly identify the boundary of field 0 and field 2 (see Figure 4) on the right side of the scan ($y \approx 415$ m). Due to the padding method, values on that boundary are simply stretched along the horizontal, often resulting in unphysical behavior on the outer sides of the LLS scans - in particular when complex flow phenomena are present near the boundaries of the LES domain. While the suggestions from above (widening the domain of the LES) would reduce these effects, as complex flow phenomena are kept further away from the boundaries of the LES domain, certainly future LLS implementations would benefit from a more complex padding method too.

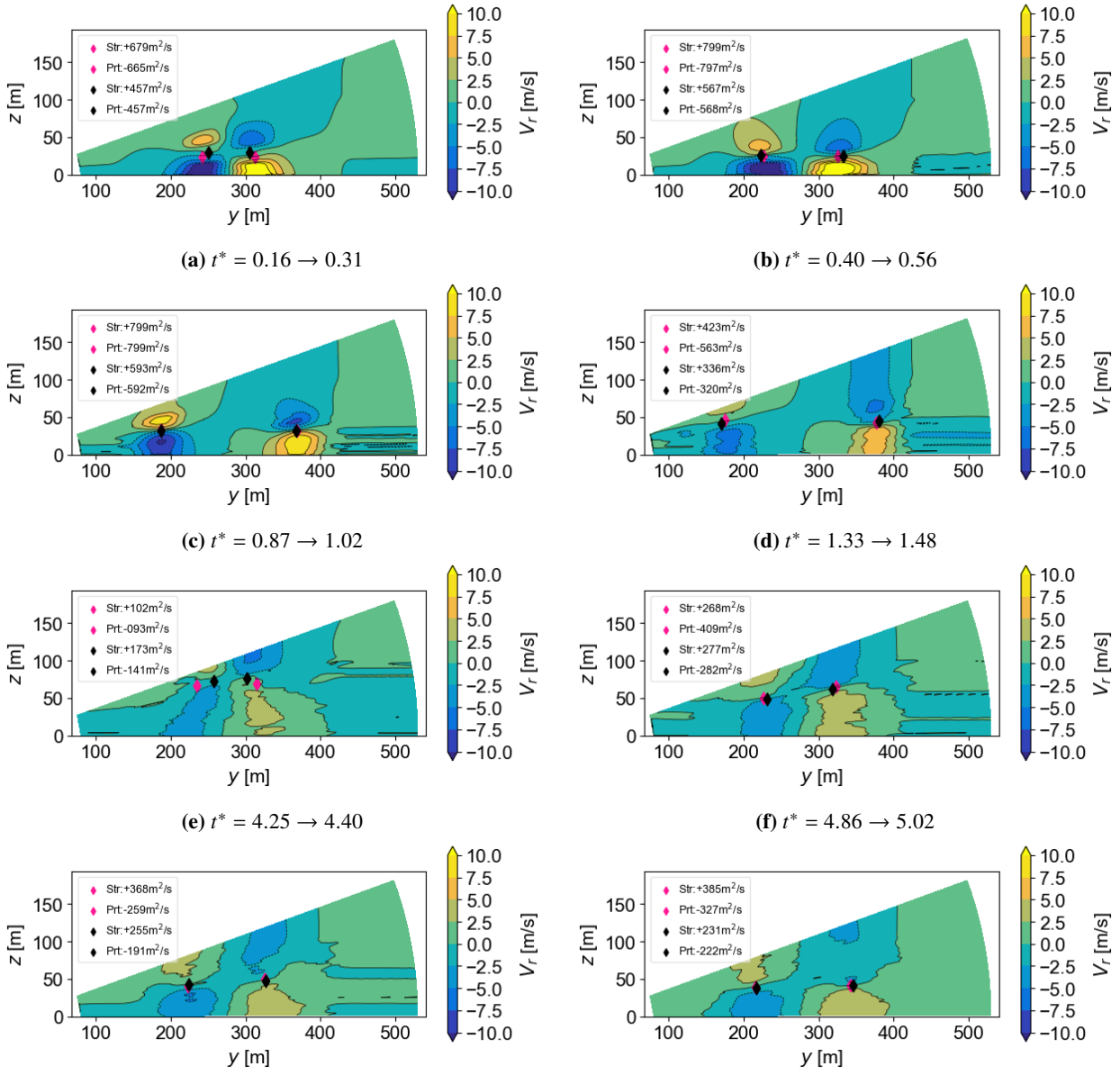

(a) $t^* = 0.16 \rightarrow 0.31$ **(b)** $t^* = 0.40 \rightarrow 0.56$

(c) $t^* = 0.87 \rightarrow 1.02$ **(d)** $t^* = 1.33 \rightarrow 1.48$

(e) $t^* = 4.25 \rightarrow 4.40$ **(f)** $t^* = 4.86 \rightarrow 5.02$

(g) $t^* = 5.33 \rightarrow 5.48$ **(h)** $t^* = 6.25 \rightarrow 6.40$

Fig. 10 Temporally evolving LLS scans for lidar position 2 and the parameters described in Table 1. Scans with the starboard (Str) and port (Prt) wake vortices are here represented in the Cartesian coordinate system. Pink and black diamonds represent the RV Method estimation and the ground-truth, respectively. Pictured LLS scans are not necessarily consecutive.

C. Investigating Errors of the Radial Velocity (RV) Method

The main objective of the LLS is the generation of highly realistic virtual lidar scans in union with the ground-truth for grading and contextualizing the error of lidar processing methods. In this work our focus is the RV method, however any lidar scan characterization method for wake vortices can be investigated in an analogue manner. LLS scans analyzed in this work originate from a single LES and thus give a first indication for the capabilities of the RV method. Future LLS work shall consider far greater sample sizes - including LES under different atmospheric conditions and aircraft landing scenarios - such that RV method errors can be reported with higher reliability and breadth.

For a qualitative comparison reconsider Figure 10. Therein the ground-truth and RV estimation are denoted by black and pink diamonds, respectively. The legend provides the associated circulations for the starboard vortex and port vortex. A quantitative comparison of the RV method with the ground-truth is given in Table 2, where the bias/systematic error (in the form of the arithmetic mean) and the statistical error (in the form of the standard deviation) in the circulation error and the localization error are given. Further, D^* is computed, representing the normalized median Euclidean distance between the vortex centers defined by the RV method and the ground-truth.

Table 2 The arithmetic mean errors (bias) of the wake vortex characterization parameters individually for the port and starboard vortex types as well as together. $+/-$ represent a higher and lower RV estimation in comparison to the ground-truth, respectively. The standard deviation of the errors is given too. In total 64 LLS scans are analyzed, they are recorded by all but virtual lidar 4 (only LLS scans where both the ground-truth and RV estimation are available are analyzed).

Vortex type	$\Delta\varphi_c$ [°]	ΔR_c [m]	D^* [-]	$\Delta\Gamma^*$ [-]	$\Delta\Gamma^*_{5-15}$ [-]
Starboard	-0.507 ± 1.805	-0.962 ± 3.769	0.075 ± 0.053	$+0.329 \pm 0.171$	$+0.269 \pm 0.159$
Port	$+0.189 \pm 0.555$	$+0.999 \pm 5.372$	0.096 ± 0.067	$+0.354 \pm 0.187$	$+0.295 \pm 0.173$
Together	-0.159 ± 1.380	$+0.019 \pm 4.743$	0.085 ± 0.061	$+0.342 \pm 0.180$	$+0.282 \pm 0.166$

First, we focus on comparing the localization capabilities of the RV method. The RV method localizes the starboard vortex with a negative bias and the port vortex with a positive bias - the starboard vortex is seen too close to the ground and the lidar, whereas the opposite is the case for the port vortex. To date it is not understood why the RV method develops these biases. Still, D^* shows that the localization capabilities of the RV method are satisfying - the error is only marginally larger than the range gate $\delta R = 3$ m. Given that the RWF of the LLS smears out the flow field according to $\hat{R} = 30$ m, it is uncertain to what extent the localization accuracy can be reduced further. We also notice that the vortex type has little influence on the error magnitude.

Second, the RV method circulation characterization is compared to the ground-truth. The circulation is overestimated for both vortex types as the bias shows. The spread of errors seem to be in reasonable bounds, suggesting the primary problem to be a systematic error. Several potential causes for this difference in circulation have been identified. One could argue that the padding approach employed in this work results in greater radial velocities near the boundaries of the LLS scans than they would be experienced in reality. However, the RV method should not be affected by the padding. The functional for circulation determination of the RV method (given by Equation 3) fits a wake vortex model using only those radial velocity values with the range gate where the vortex center was found in the previous RV method step (only the elevation angle varies). It could also be argued that the stretching of the vortices, as seen in Figure 8 and described in [43], could cause an overestimation of the vortex strength by the RV method. However, the LLS scans analyzed include scans of both increasing and decreasing φ fashion, which we assume makes this effect negligible for the circulation. Furthermore, even in LLS scans of decreasing φ fashion, the RV method estimates higher vortex strengths compared to the ground-truth. Another reason for the discrepancy could be that the RV method seeks to find the asymptotic circulation Γ_∞ at r_∞ from the vortex core center, whereas the ground-truth is found for Γ_{5-15} which naturally has a smaller value. The rightmost column of Table 2 therefore includes transformed RV circulations. Both the systematic and statistical errors decrease in comparison to the asymptotic value, still differences to the ground-truth are significant. Further investigations are required to understand the discrepancy in the circulation characterization.

For comparing the herein found accuracy of the RV method, the practical error, with the theoretical error, we necessitate the RMSE of the wake vortex characterization parameters. Table 3 shows the practical and theoretical errors of the RV method side by side. Note that we only compare parameters which the RV method inherently computes, thus neither D nor $\Delta\Gamma_{5-15}$ are given. A normalization is also not performed for this comparison. We observe that in practice all parameters are characterized with a lower accuracy. The elevation angle is $\sim$ 6.5x higher, the range is $\sim$ 2.5x

higher, and the circulation is ∼ 16x higher than theory suggests. Further theoretical error values for different (higher) CNR values are given in [10]. These additional theoretical errors are all lower than the herein shown theoretical errors. While practical errors are always expected to be larger than theoretical errors, the magnitude difference for some of these parameters is significant and cannot originate solely from flow field smearing out effects by the lidar. However, as described in Section III.B, stretching of vortices caused by their movement and LOS being recorded at different points in time, can cause a falsification of the vortex position in comparison to the LES which can observe vortices instantaneously. Although both increasing and decreasing φ LLS scans exist, for the localization this effect may not be negligible. Additional investigations, covering a wide spectrum of LLS scans, are required to verify the presented practical errors.

Table 3 The practical (from the LLS) and theoretical (from [10]) RMSEs of the wake vortex characterization parameters are given. The theoretical error is given for a CNR of 0.05, theoretical errors for further CNR values can be found in [10]. Vortex types are not differentiated. In total 64 LLS scans are analyzed, they are recorded by all but virtual lidar 4 (only LLS scans where both the ground-truth and RV estimation are available are analyzed).

Error type	$\Delta\varphi_c$ [°]	ΔR_c [m]	$\Delta\Gamma$ [m^2/s]
Practical	1.39	4.7	167.3
Theoretical	0.21	1.8	10.3

IV. Conclusions

Within a RANS-LES coupled landing simulation of a long range aircraft at high-lift configuration, five virtual Light Distance and Ranging (lidar) instruments are simulated such that the accuracy of wake vortex characterization algorithms for lidar measurements, such as the Radial Velocity (RV) method, can be investigated and quantified. With real lidar measurements no ground-truth is available such that error values are limited to theoretical estimations. Instead, the LES Lidar Simulator (LLS) is directly embedded in the RANS-LES simulation, allowing for highly realistic lidar scans to be generated with full knowledge of the wake vortex characteristics.

To simulate lidar scans, velocity components of the LES are projected onto the Lines of Sight (LOS) as they would exist if a laser beam would be shot from a specific lidar position along the runway into the surrounding atmosphere in a Range Height Indicator (RHI) scan. Given that lidar scans are not instantaneous snapshots, several LES timesteps are required between LOS recordings. In the effort to efficiently make use of computing resources, a padding algorithm is employed, allowing the virtual lidar to be placed outwith the domain of the LES. When all required velocity projections for the desired RHI scan have been conducted, a Range Gate Weighting Function (RWF) is employed across each range gate to simulate volume averaging and reconstruction over the scanning volume. Vortex tracking methods within the LES allow complete knowledge of the wake vortex characteristics at any given point in space and time within the domain, herein both vorticity and pressure play a key role in determining the ground-truth.

LLS scans generated at five different positions along the flight direction within the RANS-LES coupled landing simulation are visualized and analyzed with a common wake vortex characterization algorithm for lidar measurements, the RV method. This method aims to characterize parameters such as the position of the vortices, as well as the their strength via the circulation value. The accuracy of algorithms such as the RV method, particularly in turbulent atmosphere, is unknown to date - the ground-truth of real lidar measurements is unavailable. Thus, usage of simulated lidar scans allows to approximate errors of methods such as the RV method, as they can be compared to the ground-truth available from the LES. In this work a stable atmosphere is simulated. The statistical error of the RV method (in comparison to the ground-truth) is far greater than previous theoretical analyses suggest. Particularly the circulation is dramatically overestimated. To date it is not fully known what the origin of this overestimation is, it cannot be ruled out that either the employed padding method, or the numerical set-up also play a role in this discrepancy.

Visualizations presented herein suggest future LLS versions to implement a more sophisticated LLS scan padding algorithm, the current approach can lead to flow phenomena close to the lateral boundaries of the LES domain being stretched to great lengths. Furthermore, upcoming numerical simulations require a wider domain for the wake vortices to fully, and solely once, undergo the typical diverging hyperbolic vortex pair movement in ground proximity. On top of this, the LLS shown in this effort can be developed further to consider effects of additional critical parameters such as the Carrier-to-Noise Ratio, often a heavy source for noise in real lidar measurements. Lastly, a multitude of additional

numerical simulations are needed to cover a wide spectrum of atmospheric conditions and landing scenarios. These should then be processed with a variety of different lidar measurement algorithms for wake vortices in order to evaluate their accuracy. Still, this first implementation of virtual lidar in LES indicates promising capabilities in evaluating wake vortex characterization methods, specifically quantifying their error magnitude. Such knowledge puts past and future studies which rely on these characterization algorithms into perspective.

Acknowledgments

This project has received funding within the framework of the Single European Sky Air Traffic Management Research Joint Undertaking "Safely Optimized Runway Throughput" project (VLD3-W2 SORT) within the European Union's Horizon 2020 Research and Innovation Programme under grant agreement no. 874520 as well as from the DLR, German Aerospace Center (DLR) project "Wetter und Disruptive Ereignisse." We also greatly acknowledge the provided computing time on the high performance computer SuperMUC-NG by Leibniz-Rechenzentrum (LRZ).

References

[1] Gerz, T., Holzäpfel, F., and Darracq, D., "Commercial aircraft wake vortices," *Progress in Aerospace Sciences*, Vol. 38, No. 3, 2002, pp. 181–208. https://doi.org/10.1016/S0376-0421(02)00004-0.

[2] Stephan, A., Rohlmann, D., Holzäpfel, F., and Rudnik, R., "Effects of detailed aircraft geometry on wake vortex dynamics during landing," *Journal of Aircraft*, Vol. 56, No. 3, 2019, pp. 974–989. https://doi.org/10.2514/1.C034961.

[3] Hallock, J. N., and Holzäpfel, F., "A review of recent wake vortex research for increasing airport capacity," *Progress in Aerospace Sciences*, Vol. 98, 2018, pp. 27–36. https://doi.org/10.1016/j.paerosci.2018.03.003.

[4] Rossow, V., and James, K., "Overview of wake-vortex hazards during cruise," *Journal of Aircraft*, Vol. 37, No. 6, 2000, pp. 960–975. https://doi.org/10.2514/2.2723.

[5] Holzäpfel, F., Stephan, A., Rotshteyn, G., Körner, S., Wildmann, N., Oswald, L., Gerz, T., Borek, G., Floh, A., Kern, C., Kerschbaum, M., Nossal, R., Schwarzenbacher, J., Strobel, M., Strauss, L., Weiß, C., Kauczok, S., Schiefer, C., Czekala, H., Maschwitz, G., and Smalikho, I., "Mitigating Wake Turbulence Risk During Final Approach via Plate Lines," *AIAA Journal*, Vol. 59, No. 11, 2021, pp. 4626–4641. https://doi.org/10.2514/1.J060025.

[6] Holzäpfel, F., Gerz, T., Frech, M., Tafferner, A., Köpp, F., Smalikho, I. N., Rahm, S., Hahn, K.-U., and Schwarz, C., "The wake vortex prediction and monitoring system WSVBS Part I: Design," *Air Traffic Control Quarterly*, Vol. 17, No. 4, 2009, pp. 301–322. https://doi.org/10.2514/atcq.17.4.301.

[7] Cheng, J., Hoff, A., Tittsworth, J., and Gallo, W. A., "The Development of Wake Turbulence Re-Categoriza-tion in the United States," *8th American Institute of Aeronautics and Astronautics Atmospheric and Space Environments Conference*, 2016, pp. 1–12. https://doi.org/10.2514/6.2016-3434.

[8] Köpp, F., Rahm, S., and Smalikho, I. N., "Characterization of aircraft wake vortices by 2-μ m pulsed Doppler lidar," *Journal of Atmospheric and Oceanic Technology*, Vol. 21, No. 2, 2004, pp. 194–206. https://doi.org/10.1175/1520-0426(2004)021<0194:COAWVB>2.0.CO;2.

[9] Banakh, V., and Smalikho, I. N., *Coherent Doppler Wind Lidars in a Turbulent Atmosphere*, Artech House, 2013.

[10] Smalikho, I. N., Banakh, V., Holzäpfel, F., and Rahm, S., "Method of radial velocities for the estimation of aircraft wake vortex parameters from data measured by coherent Doppler lidar," *Optics Express*, Vol. 23, No. 19, 2015, pp. A1194–A1207. https://doi.org/10.1364/OE.23.0A1194.

[11] Smalikho, I. N., and Banakh, V., "Estimation of aircraft wake vortex parameters from data measured with a 1.5-μ m coherent Doppler lidar," *Optics letters*, Vol. 40, No. 14, 2015, pp. 3408–3411. https://doi.org/10.1364/OL.40.003408.

[12] Weijun, P., Yingjie, D., Qiang, Z., Jiahao, T., and Jun, Z., "Deep Learning for Aircraft Wake Vortex Identification," *IOP Conference Series: Materials Science and Engineering*, Vol. 685, IOP Publishing, 2019, pp. 1–8. https://doi.org/10.1088/1757-899x/685/1/012015.

[13] Baranov, N., and Resnick, B., "Wake Vortex Detection by Convolutional Neural Networks," *International Journal of Electrical Engineering and Computer Science (EEACS)*, Vol. 3, 2021, pp. 92–97.

[14] Wartha, N., Stephan, A., Holzäpfel, F., and Rotshteyn, G., "Characterizing aircraft wake vortex position and strength using LiDAR measurements processed with artificial neural networks," *Opt. Express*, Vol. 30, No. 8, 2022, pp. 13197–13225. https://doi.org/10.1364/OE.454525, URL http://opg.optica.org/oe/abstract.cfm?URI=oe-30-8-13197.

[15] Stephan, A., Holzäpfel, F., and Misaka, T., "Hybrid simulation of wake-vortex evolution during landing on flat terrain and with plate line," *International Journal of Heat and Fluid Flow*, Vol. 49, 2014, pp. 18–27. https://doi.org/10.1016/j.ijheatfluidflow.2014.05.004.

[16] Manhart, M., "A zonal grid algorithm for DNS of turbulent boundary layers," *Computers & Fluids*, Vol. 33, No. 3, 2004, pp. 435–461. https://doi.org/10.1016/S0045-7930(03)00061-6.

[17] Meneveau, C., Lund, T. S., and Cabot, W. H., "A Lagrangian dynamic subgrid-scale model of turbulence," *Journal of fluid mechanics*, Vol. 319, 1996, pp. 353–385. https://doi.org/10.1017/S0022112096007379.

[18] Hokpunna, A., and Manhart, M., "Compact fourth-order finite volume method for numerical solutions of Navier–Stokes equations on staggered grids," *Journal of Computational Physics*, Vol. 229, No. 20, 2010, pp. 7545–7570. https://doi.org/10.1016/j.jcp.2010.05.042.

[19] Hokpunna, A., "Compact fourth-order scheme for numerical simulations of Navier-Stokes equations," Ph.D. thesis, Technische Universität München, 2009.

[20] Misaka, T., Holzapfel, F., and Gerz, T., "Wake evolution of high-lift configuration from roll-up to vortex decay," *51st AIAA Aerospace Sciences Meeting including the New Horizons Forum and Aerospace Exposition*, 2013, p. 362. https://doi.org/10.2514/6.2013-362.

[21] Stumpf, E., "Study of four-vortex aircraft wakes and layout of corresponding aircraft configurations," *Journal of aircraft*, Vol. 42, No. 3, 2005, pp. 722–730. https://doi.org/10.2514/1.7806.

[22] Holzäpfel, F., Gerz, T., and Baumann, R., "The turbulent decay of trailing vortex pairs in stably stratified environments," *Aerospace Science and Technology*, Vol. 5, No. 2, 2001, pp. 95–108. https://doi.org/10.1016/S1270-9638(00)01090-7.

[23] Misaka, T., Holzäpfel, F., Hennemann, I., Gerz, T., Manhart, M., and Schwertfirm, F., "Vortex bursting and tracer transport of a counter-rotating vortex pair," *Physics of Fluids*, Vol. 24, No. 2, 2012, p. 025104. https://doi.org/10.1063/1.3684990.

[24] Fujii, K., "Unified zonal method based on the fortified solution algorithm," *Journal of Computational Physics*, Vol. 118, No. 1, 1995, pp. 92–108. https://doi.org/10.1006/jcph.1995.1082.

[25] Keye, S., "Fluid-structure coupled analysis of a transport aircraft and flight-test validation," *Journal of Aircraft*, Vol. 48, No. 2, 2011, pp. 381–390. https://doi.org/10.2514/1.C000235.

[26] Hah, C., and Lakshminarayana, B., "Measurement and prediction of mean velocity and turbulence structure in the near wake of an airfoil," *Journal of Fluid Mechanics*, Vol. 115, 1982, pp. 251–282. https://doi.org/10.1017/S0022112082000743.

[27] Hennemann, I., "Deformation und Zerfall von Flugzeugwirbelschleppen in turbulenter und stabil geschichteter Atmosphäre," Ph.D. thesis, Technische Universität München, 2010.

[28] Stephan, A., "Wake Vortices of Landing Aircraft," Ph.D. thesis, Ludwig-Maximilians-Universität München, 2014. DLR Forschungsbericht 2014-10.

[29] Holzäpfel, F., Gerz, T., Köpp, F., Stumpf, E., Harris, M., Young, R. I., and Dolfi-Bouteyre, A., "Strategies for circulation evaluation of aircraft wake vortices measured by lidar," *Journal of Atmospheric and Oceanic Technology*, Vol. 20, No. 8, 2003, pp. 1183–1195. https://doi.org/10.1175/1520-0426(2003)020<1183:SFCEOA>2.0.CO;2.

[30] Sallab, A. E., Sobh, I., Zahran, M., and Essam, N., "LiDAR Sensor modeling and Data augmentation with GANs for Autonomous driving," *arXiv preprint arXiv:1905.07290*, 2019.

[31] Manivasagam, S., Wang, S., Wong, K., Zeng, W., Sazanovich, M., Tan, S., Yang, B., Ma, W.-C., and Urtasun, R., "Lidarsim: Realistic lidar simulation by leveraging the real world," *Proceedings of the IEEE/CVF Conference on Computer Vision and Pattern Recognition*, 2020, pp. 11167–11176.

[32] Robey, R., and Lundquist, J. K., "Behavior and mechanisms of Doppler wind lidar error in varying stability regimes," *Atmospheric Measurement Techniques*, Vol. 15, No. 15, 2022, pp. 4585–4622. https://doi.org/10.5194/amt-15-4585-2022.

[33] Aitken, M. L., Rhodes, M. E., and Lundquist, J. K., "Performance of a wind-profiling lidar in the region of wind turbine rotor disks," *Journal of Atmospheric and Oceanic Technology*, Vol. 29, No. 3, 2012, pp. 347–355. https://doi.org/10.1175/JTECH-D-11-00033.1.

[34] Boquet, M., Royer, P., Cariou, J.-P., Machta, M., and Valla, M., "Simulation of Doppler lidar measurement range and data availability," *Journal of Atmospheric and Oceanic Technology*, Vol. 33, No. 5, 2016, pp. 977–987. https://doi.org/10.1175/JTECH-D-15-0057.1.

[35] Rösner, B., Egli, S., Thies, B., Beyer, T., Callies, D., Pauscher, L., and Bendix, J., "Fog and Low Stratus Obstruction of Wind Lidar Observations in Germany—A Remote Sensing-Based Data Set for Wind Energy Planning," *Energies*, Vol. 13, No. 15, 2020, p. 3859. https://doi.org/10.3390/en13153859.

[36] Frehlich, R., "Effects of wind turbulence on coherent Doppler lidar performance," *Journal of Atmospheric and Oceanic Technology*, Vol. 14, No. 1, 1997, pp. 54–75. https://doi.org/10.1175/1520-0426(1997)014<0054:EOWTOC>2.0.CO;2.

[37] Gryning, S.-E., Mikkelsen, T., Baehr, C., Dabas, A., Gómez, P., O'Connor, E., Rottner, L., Sjöholm, M., Suomi, I., and Vasiljević, N., "Measurement methodologies for wind energy based on ground-level remote sensing," *Renewable Energy Forecasting*, Elsevier, 2017, pp. 29–56. https://doi.org/10.1016/B978-0-08-100504-0.00002-0.

[38] Simley, E., Fürst, H., Haizmann, F., and Schlipf, D., "Optimizing Lidars for wind turbine control applications—Results from the IEA wind task 32 Workshop," *Remote Sensing*, Vol. 10, No. 6, 2018, p. 863. https://doi.org/10.3390/rs10060863.

[39] Banakh, V., Smalikho, I., Köpp, F., and Werner, C., "Turbulent Energy Dissipation Rate Measurement Using Doppler Lidar," *Advances in Atmospheric Remote Sensing with Lidar: Selected Papers of the 18th International Laser Radar Conference (ILRC), Berlin, 22–26 July 1996*, Springer, 1997, pp. 255–258. https://doi.org/10.1007/978-3-642-60612-0_63.

[40] Breitsamter, C., "Wake vortex characteristics of transport aircraft," *Progress in Aerospace Sciences*, Vol. 47, No. 2, 2011, pp. 89–134. https://doi.org/10.1016/j.paerosci.2010.09.002.

[41] Harvey, J., and Perry, F. J., "Flowfield produced by trailing vortices in the vicinity of the ground," *AIAA journal*, Vol. 9, No. 8, 1971, pp. 1659–1660. https://doi.org/10.2514/3.6415.

[42] Spalart, P., Strelets, M. K., Travin, A., and Shur, M., "Modeling the interaction of a vortex pair with the ground," *Fluid Dynamics*, Vol. 36, No. 6, 2001, pp. 899–908. https://doi.org/10.1023/A:1017958425271.

[43] Smalikho, I., "Taking into account the ground effect on aircraft wake vortices when estimating their circulation from lidar measurements," *Atmospheric and Oceanic Optics*, Vol. 32, 2019, pp. 686–700. https://doi.org/10.1134/S1024856019060149.